



Full length article

## Entrained flow gasification: Impact of fuel spray distribution on reaction zone structure

Manuel Haas<sup>a,\*</sup>, Maximilian Dammann<sup>a,b,c</sup>, Sabine Fleck<sup>a</sup>, Thomas Kolb<sup>a,b</sup>

<sup>a</sup> Karlsruhe Institute of Technology (KIT), Institute for Technical Chemistry, Gasification Technology (ITC vgt), Herrmann-von-Helmholtz-Platz 1, 76344 Eggenstein-Leopoldshafen, Germany

<sup>b</sup> Karlsruhe Institute of Technology (KIT), Engler-Bunte-Institute, Fuel Technology (EBI ceb), Engler-Bunte-Ring 1, 76131 Karlsruhe, Germany

<sup>c</sup> Clausthal University of Technology, Institute for Energy Process Engineering and Fuel Technology (IEVB), Agricolastrasse 4, 38678 Clausthal-Zellerfeld, Germany



### ARTICLE INFO

#### Keywords:

Entrained flow gasification  
Flame structure  
Laser induced fluorescence  
Free jet  
CFD  
Inverse diffusion flame

### ABSTRACT

Entrained flow gasification (EFG) is an important process for generating syngas from biogenic and anthropogenic waste based feedstocks for a future circular economy. The EFG process is characterized by complex interactions between different physical and thermo-chemical sub processes which determine syngas quality and process efficiency. The understanding of these sub processes is essential for the development of validated models, and therefore for design and scale up of EFG reactors. EFG processes using a central jet burner configuration feature flames that can be described as inverse diffusion flames superimposed by a fuel spray. The flames are characterized by (i) the conversion of liquid and slurry droplets and (ii) the oxidation of recirculating synthesis gas with the gasification medium. This work studies the interactions between fuel and oxidizer in the near-flame region of an atmospheric EFG process. The model fuel ethylene glycol was gasified using oxygen-enriched air for two different burner nozzle configurations. Spray imaging, OH-LIF and Fuel Tracer-LIF measurements were carried out in addition to gas temperature measurements to characterize the fuel distribution and the flame structure. The experimental results show that narrower fuel spray distributions result in shorter flames and changes in flame shape from a compact to a hollow cone shape in the downstream flame region. The experiments were accompanied by 2-phase free-jet modeling and RANS based CFD modeling. The models were improved to reflect the experimental findings including the fuel spray distributions. The simulation results predict the observed flame structures well using both models and for both burner nozzle configurations. The changes in flame structure for different spray distributions can be explained by local stoichiometry using the results of the 2-phase free-jet model.

### 1. Introduction

The challenge of creating a CO<sub>2</sub> neutral economy requires not only a net-zero CO<sub>2</sub> energy system but also a shift towards a circular economy. Processes for conversion of low grade biogenic and anthropogenic feedstocks are needed to enable a sustainable energy system together with a closed anthropogenic carbon cycle. High-pressure entrained flow gasification for the conversion of waste based feedstocks into new high-quality products can serve as an enabling technology for this transition due to its high fuel flexibility and its capability to produce a high-quality synthesis gas suitable for chemical synthesis.

The Entrained Flow Gasification (EFG, see Table 3) process is characterized by complex interactions of physical and thermo-chemical sub-processes [1,2]. Understanding these processes is essential for design and scale-up and for the efficient, feedstock flexible operation of EFG reactors. Particularly, the processes in the burner near region

which determine fuel conversion and therefore syngas quality and process efficiency need a better understanding for optimum design of burner and adjustment of operational parameters. The goal of this study is to provide insight in the interaction between fuel and oxidizer medium in the near-flame region of an atmospheric EFG reactor to gain both fundamental knowledge of the fuel conversion processes in EFG flames and deliver information for EFG burner development.

#### 1.1. Research on flames in technical EFG systems

Only a limited number of experimental studies have dealt with the flame structure in EFG processes. In addition to (i) invasive concentration and temperature measurements in the far-flame region [2–4], (ii) local heat flux measurements at the reactor wall [5] and (iii) non spatially resolved spectroscopy [6,7], more advanced optical diagnostics

\* Corresponding author.

E-mail address: [manuel.haas@kit.edu](mailto:manuel.haas@kit.edu) (M. Haas).

<https://doi.org/10.1016/j.fuel.2022.126572>

Received 19 August 2022; Received in revised form 13 October 2022; Accepted 28 October 2022

Available online 30 November 2022

0016-2361/© 2022 The Author(s). Published by Elsevier Ltd. This is an open access article under the CC BY-NC-ND license (<http://creativecommons.org/licenses/by-nc-nd/4.0/>).

like (iv) camera-based systems to investigate spray behavior [8,9], (v) particle image velocimetry (PIV) to measure velocity fields [10,11], (vi) absorption spectroscopy for gas temperature and concentration measurement [12–15] and (vii) chemiluminescence imaging for reaction zone mapping [16–18] were applied to EFG systems. However, most of these studies focused on single effects like flame lift-off distance, temperature field or particle dispersion, which makes it difficult to derive an overall process understanding.

The flame structure of EFG and similar systems was also investigated using CFD simulations. For example, [19–21] compared near-flame and far-flame predictions for different burner configurations demonstrating the significance of the burner design for fuel conversion. However, validation was only performed with respect to the far-flame predictions. RANS based and large eddy simulations for the gasification of the model fuel mono ethylene glycol provided far-flame predictions that were in good agreement with experimental results but deviated significantly in the prediction of flame shape [22,23], showing the importance of the numerical description of turbulent mixing of fuel, synthesis gas and oxidizer. In addition, the fuel spray distribution in the flame zone was also found to be decisive [24] for the prediction of flame structure.

### 1.2. Flame types in EFG

In commercial EFG reactors, fuel and gasification medium, usually consisting of oxygen and steam, are typically fed to the reaction chamber by coannular external mixing burner nozzles [25]. Different burner designs with varying arrangements of the inlet streams are in use. In this work, burner nozzles with a central liquid fuel stream surrounded by a coannular oxidizer stream are applied. The resulting flame can be described as an inverse diffusion flame (IDF) of oxygen rich gasification medium issuing into a hot syngas atmosphere as a gas free jet which is superimposed by a coflowing spray of liquid fuel droplets. The oxygen in the jet medium is primarily consumed by reaction with syngas entrained from the surrounding atmosphere and to a lesser degree by reaction with fuel vapor and its decomposition products. Fuel droplets are converted partly in the flame zone where oxygen is still present, but also in the oxygen free atmosphere surrounding the flame. The interaction of the fuel droplets with the oxidizer influences flame structure and is therefore one key aspect to understanding the fuel conversion processes in EFG.

Recently, IDFs gained research interest and there have been numerous studies on laboratory systems under well defined conditions outlined in the review by Zhen et al. [26]. Most of the published work however focuses on stoichiometric or lean IDFs with air and is due to high  $N_2$ -dilution of minor relevance for gasification conditions. Numerous publications looked into the role of oxygen enrichment in technical [27–29] and laboratory [30] combustion systems, but they typically do not feature rich conditions or an inverse flame configuration.

Notable work on rich IDFs is provided by [31–33] for laminar and [34,35] for turbulent IDFs. The latter one especially focus on the qualitative distribution of temperature and OH radicals in an oxygen enriched turbulent IDF in comparison to a normal diffusion flame (NDF) under equivalent flow conditions. Stelzner et al. [31] measured gas temperature by OH LIF to investigate the relation between OH concentration and temperature for a rich, oxygen enriched laminar IDF and shows that under these conditions very high temperatures up to 3000 K are possible. To the author's knowledge, the superposition of an IDF with a liquid fuel spray is not covered by experimental work on model systems to date, thus the interaction between the IDF and the fuel requires more research.

### 1.3. Flame structure analysis

For flame structure analysis, the OH radical has been used as a flame front marker for decades particularly because of its good detectability by laser induced fluorescence (LIF) [36–39]. The OH radical

is produced during oxidation processes and marks the transition from unburnt to burnt gases in the flame [39,40]. OH is typically present in high concentrations in the flame front itself and can also be found in equilibrium concentrations in hot product gases. Under non premixed conditions OH is mostly found at the interface between oxidizer and fuel gas [41–43], which is also true for rich inverse diffusion flames [35]. This makes OH a suitable spatial marker for the high temperature oxidation processes in the flames covered in this work. Without further information on other intermediates, the suitability of OH alone as a marker for heat release is limited, as discussed by [44]. The OH LIF signal is generally dependent on local concentration of other main species due to quenching of the excited states [36,38]. Most studies including the present one therefore focus on the qualitative interpretation of OH LIF signals as markers for flame front location and reaction intensity instead of discussing quantitative OH concentrations.

Based on the LIF measurements described in Section 2.2, three reaction zones are defined in this work for flame structure analysis (Section 3.2). Reaction zones in entrained flow gasification have been discussed in previous works [2,23], which will be expanded in this paper. The core zone of the flame (CZ) is defined as the area close to the nozzle exit at the jet axis where fuel but no OH can be detected. The situation in the core zone is characterized by the presence of fuel droplets and gasification medium at low temperature conditions where no oxidation reaction takes place yet. It is indicated by the absence of OH. The oxidation zone (OZ) is defined as the region enveloping the core zone where OH is present. In this zone, oxygen rich gasification medium is consumed by reaction with syngas entrained by the gas jet from the recirculation zone as well as with fuel vapor originating from the central fuel spray. The oxidation reactions lead to heat release resulting in high temperatures and also to formation of OH radicals. The gasification zone (GZ) is defined as the region surrounding the oxidation zone. Oxygen from the gasification medium is not present, fuel droplets and vapor are converted under moderately high temperature by slow gasification reactions, OH is no longer detected.

### 1.4. Experimental and numerical approach

The objectives of this study are to show the influence of the liquid fuel spray distribution on an inverse diffusion flame in an EFG system in order to gain a deeper understanding of the fuel conversion processes and the interaction between fuel and oxidizer under gasification conditions. An optically accessible atmospheric entrained flow gasifier was used as a model system for high pressure entrained flow gasification, since access for detailed diagnostics is limited in the pressurized system. The detailed process understanding derived at the atmospheric system can then be transferred to pressurized systems where macroscopic effects can be validated.

In the atmospheric gasifier, two central liquid jet burner nozzles were applied, providing different radial spray distributions under otherwise identical operating conditions. Sprays and flame structures in the gasification experiments were investigated by OH LIF and fuel tracer LIF, spray imaging and temperature measurement. The measurements were complemented by atmospheric atomization experiments and by numerical simulation using a 2-Phase Free-Jet Model (2-Ph-FJM) and a RANS based CFD model. The original two-phase free-jet model [18,45] and the original CFD model [22,24,46–49] were revised within this work to improve the fuel spray distribution and were subsequently applied for the simulation of the gasification experiments. The 2-Ph-FJM was also used to investigate and interpret the influence of the fuel spray distribution on the experimentally observed flame length and flame shape. The CFD model was used to support the explanation provided by the 2-Ph-FJM and to further investigate the role of fuel evaporation in the flames considered.

The adapted models are described alongside the experimental methods in Section 2. The experimental and numerical results are subsequently presented and discussed in Section 3. The main conclusions are given in Section 4.

**Table 1**  
Nozzle geometry parameters.

Nozzle	$\frac{d_{liq}}{mm}$	$\frac{s}{mm}$	$\frac{d_{gas}}{mm}$	$\frac{\alpha_{gas}}{\circ}$
D1.1	2	0.5	7.12	30
D2.1	2	0.5	5.25	30

**Table 2**  
Experimental conditions of the atmospheric gasification experiments.

Case	Nozzle	REGA experiment	GLR	$\frac{\dot{m}_{fuel}}{kg/h}$	$\frac{\dot{m}_{air}}{kg/h}$	$\frac{\dot{m}_{O_2}}{kg/h}$	$\frac{u_{gas,0}}{m/s}$
A	D1.1	TUC5 V1374	0.83	12.42	3.77	6.55	69
B	D2.1	TUC5 V1105	0.83	12.42	3.77	6.55	156

**Table 3**  
List of acronyms.

Acronyms	Explanation
ATMO	Atmospheric spray test rig
CFD	Computational fluid dynamics
EFG	Entrained flow gasification
GGPD	Generalized Gaussian probability density
GMBS	Generalized member-ship bell-shaped
GLR	Gas to liquid ratio
IDF	Inverse diffusion flame
L	Logistic
LIF	Laser induced fluorescence
MEG	Mono ethylene glycol
PPDS	Physical Property Data Services
RANS	Reynolds averaged Navier–Stokes
REGA	Research entrained flow gasifier
2-Ph-FJM	2-phase free jet model

## 2. Methods

This section describes the experimental and the numerical methods applied within this work.

### 2.1. Gasification experiments

Gasification experiments were carried out at the atmospheric Research Entrained flow Gasifier REGA, which is described in detail in [2]. On the measurement plane E0, the reactor provides 4 access ports (see Fig. 1) that can be equipped with nitrogen-flushed quartz-glass windows to provide optical access to the reaction chamber. The burner plate is movable in axial direction to enable analytical and optical access in a range of 0–300 mm nozzle distance at E0. Two external mixing twin fluid nozzles were applied (see Fig. 1) with geometry parameters given in Table 1.

The reference fuel mono ethylene glycol (MEG) was gasified with an  $O_2/N_2$  mixture under the conditions given in Table 2, corresponding to an adiabatic equilibrium temperature of 1700 °C. The model fuel is chosen due to its similarity to biogenic pyrolysis oil as described in [2]. For each nozzle geometry, a set of experimental data was acquired (cases A and B). In successive experiments, data on OH and fuel distribution, spray patterns and temperature profiles were measured. OH-LIF and fuel tracer-LIF data were measured in the range of 0–300 mm nozzle distance. The setup of this experiment is described in detail in Section 2.2. Spray breakup images for 0–40 mm nozzle distance were taken with the same setup. Radial temperature profiles were measured at nozzle distances of 150, 200 and 300 mm (case B) and 300 mm (case A). A method for correction of radiation using double bead thermocouples described in [2] was applied.

### 2.2. LIF measurements

Simultaneous qualitative OH-LIF and fuel tracer-LIF imaging experiments were conducted with the setup shown in Fig. 1. A pulsed,

frequency doubled Nd:YAG laser (Quanteq Q-smart 850) with a wavelength of 532 nm was used to pump a frequency doubled dye laser (Sirah Cobra-Stretch) with an output wavelength of 283 nm. The laser beam was expanded by a cylindrical lens followed by a collimation optics to form a laser sheet with a height of 50 mm and a width of 0.5 mm at the measurement position. The pulse energy after the collimation optics was determined to be approximately 10 mJ with a pulse rate of 10 Hz. Images were acquired with an intensified CMOS camera system (LaVision IRO coupled with LaVision Imager M-lite 2M) which was equipped with a stereoscope to allow simultaneous measurements of OH- and Fuel Tracer-LIF. Both optical channels were aligned by a calibration plate prior to the measurement to ensure a spatial overlap of the images. To suppress background radiation, the intensifier gain was set to 50 ns. Detection of the OH radical was performed with a 320 nm / 40 nm FWHM bandpass filter while the fuel tracer channel was equipped with a 572 nm / 33 nm FWHM bandpass filter. Rhodamine 6G was dissolved in MEG as a fuel tracer. The concentration of  $10^{-5}$  mol/L was chosen to get comparable signal intensities in the OH and Fuel Tracer channel without saturating the image intensifier.

In order to minimize temperature dependence of the OH signal, the dye laser output was tuned to the  $Q_1(8)$ -line in the A-X (1,0)-band of the OH radical at 283.55 nm [50]. The line position was verified by comparing a measured excitation spectrum to a spectrum calculated using LIFBASE [51]. In addition, off line images with laser excitation at 283.51 nm and background images without laser excitation were taken. The experiments were repeated without addition of fuel tracer to account for spectral crosstalk between Rhodamine 6G and OH. The final OH images shown in this work were taken from this dataset. A quenching correction for OH was not performed due to lack of detailed gas concentration data.

The burner was moved in 20 mm steps. 500 images were taken at each position to get a stable time average, which was assessed in a sensitivity study. The single images were averaged and corrected with the respective background image, followed by a white image correction and a correction for spatial inhomogeneities in the laser sheet profile. The 20 mm image segments of each burner position were merged to yield an intensity distribution of the whole flame area.

### 2.3. Atomization experiments

Spray characterization experiments under ambient conditions were carried out at the atmospheric spray test rig (ATMO) described in [52]. MEG was atomized with air at input conditions analogous to the conditions given in Table 2. Radial profiles of droplet size and velocity at a nozzle distance of 100 mm were measured with a PDA system described in [18]. PDA data processing and calculation of the Sauter mean diameter was performed with the SprayCat toolbox presented in [53,54]. Spray formation and liquid jet breakup was analyzed using a high speed camera system described in [54]. 2000 images with a frame rate of 3600 Hz were recorded for each nozzle to obtain a representative dataset. In addition, radial liquid mass flux density distribution was measured in a nozzle distance of 100 mm by the method specified in 2.4.

### 2.4. Patternator experiments

A mechanical spray patternator was used for mass flux density measurements in the atmospheric atomization experiments. The patternator is a linear array of 62 chambers with a length of 6.2 mm, a width of 4.9 mm and a height of 150 mm, which are each separated by 0.25 mm. The patternator was placed in the spray cone at a nozzle distance of 100 mm and uncovered for a specific period of time. The mass flux density in a chamber was determined by the collected fluid volume per unit

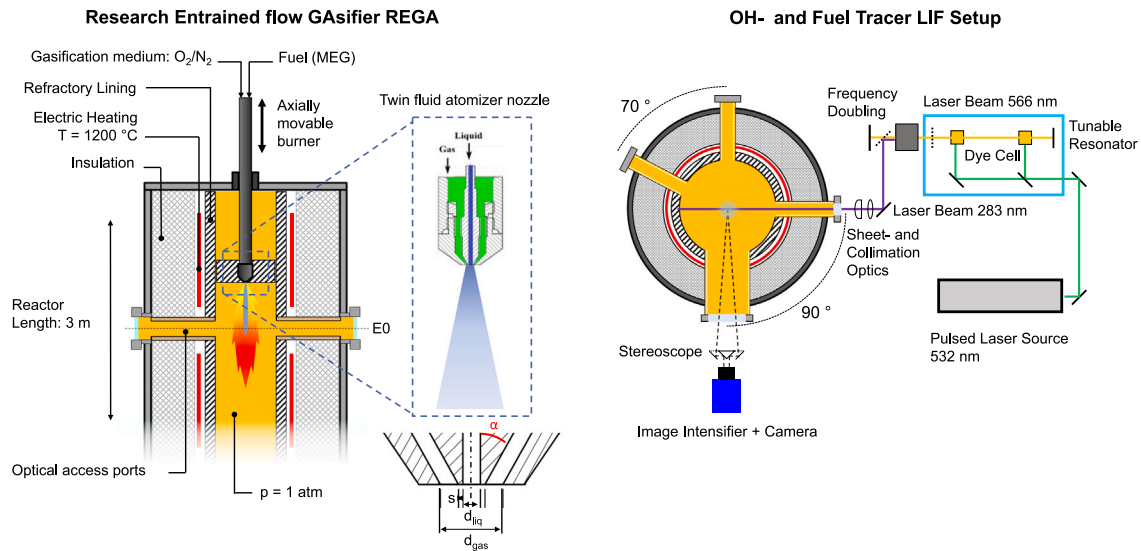


Fig. 1. REGA test rig cross sections and nozzle configuration (left) and LIF setup (right).

time. Three mass flux density profiles were measured for each nozzle and averaged. The profiles were fitted by a logistic peak function

$$\dot{m}_{liq} = A \cdot \frac{e^{-z}}{(1 + e^{-z})^2}, \text{ where } z = \frac{r - \Delta r}{w} \quad (1)$$

which is used for a mass balance by radial integration to validate the measurement. As a characteristic parameter, the full angle containing 90% of the spray mass flow is defined based on the cumulative radial mass flow distribution.

$$\theta_{0.9} = 2 \cdot \arctan\left(\frac{r_0}{z}\right), \text{ with } \frac{\dot{M}_{liq}(r_0)}{\dot{M}_{liq}(r = \infty)} = 0.9 \quad (2)$$

## 2.5. 2-phase free jet model

The 2-phase free jet model (2-Ph-FJM) was adopted from preceding works [18,45] but adapted with respect to the radial liquid mass flow distribution. The model describes steady state fields of mixture fraction and gas and droplet velocities for a two phase free jet. It uses sub-process models for droplet evaporation and gas phase reaction to describe fuel conversion. Equations for the single-phase free jet are modified to reflect the two phase case based on theoretical considerations and experimental data.

Exchange of momentum and mass are governed by the momentum of the free jet at the nozzle exit, which is a key parameter for the similarity relations of gas free jets. Since the gas phase is injected through an annulus in the burner nozzles used in this work, the flow is assumed to enter the reaction chamber by a circular cross section with the same momentum and mass flow as in the original geometry, resulting in a geometric equivalent nozzle diameter given by

$$d_{eq} = \sqrt{\frac{4 \cdot A_{gas}}{\pi}} \quad (3)$$

In the model, the liquid phase is introduced into the gas flow in a grid of angular discretized radial segments, which leads to droplets moving along straight trajectories with fixed angles originating from the nozzle exit. In the original 2-Ph-FJM, liquid mass flow is distributed over the radial segments proportionally to the gas mass flow given by the free jet equations, i.e. the local gas-to-liquid-ratio in each radial segment  $i$

$$GLR_{local,i} = \frac{\dot{M}_{gas,i}}{\dot{M}_{liq,i}} \quad (4)$$

is originally set constant and thus equal to the global  $GLR$ . Based on the results of the experiments described, the model was modified in this work to reflect the observed fuel mass flow distributions (see Sections 2.4 and 3.1). The cumulative mass flow distributions derived from the patterator experiments were used as input for the model. The amplitude of the distribution was modified to account for the mass balance error. Mass flow rate distribution in the model is based on this data, leading to a radial  $GLR_{local}$ -profile. Calculated mass flux densities for the ambient case were validated with the spray data derived from the ambient atomization experiments.

Radial distribution of droplet size was also implemented in this work in contrast to the previous model using the spray data from the ambient experiment (Sections 2.4 and 3.1). The experimental radial Sauter mean diameter distributions were nondimensionalized and approximated with a 4th-order polynomial. In each radial segment, a Weibull  $Q_3$ -distribution with a sauter mean diameter corresponding to the approximation function was used to define 50 equally spaced droplet size classes.

Coefficients for turbulent exchange of momentum and mass in the 2-phase free-jets were defined according to [55] based on the results of the spray characterization experiments. The expansion of the gas jet due to the outer recirculation zone of the REGA setup is considered in accordance with the descriptions given by [56,57] to account for the increased gas jet angle.

To assess the influence of fuel evaporation on the flame, local absolute stoichiometry in the gas phase was calculated by

$$\lambda_{abs} = \frac{n_O}{2 \cdot n_C + 0.5 \cdot n_H} \quad (5)$$

as discussed by [2].

The cases A and B were simulated under the given model assumptions using the input data presented in Sections 2.1 and 3.1. Additionally, a parameter variation to investigate the influence of the radial spray distribution was conducted (see Section 3.3.1).

## 2.6. CFD model

The CFD model for the gasification of ethylene glycol [22,46–49] was recently presented in detail [24] and partially revised within this work. The model is used for steady-state simulations of the REGA reactor using ANSYS Fluent [58] and user-defined implementations. The gas phase is described in the Eulerian specification of reference using the RANS approach. Favre averaged Navier–Stokes equations, Favre averaged species balance equations and the turbulence equations

of the SST  $k - \omega$  model [59,60] are solved on two-dimensional and axisymmetric domains with approximately  $2 \cdot 10^5$  unstructured cells using the finite-volume method and the SIMPLEC algorithm [61]. The second-order upwind scheme is used for the discretization of the momentum, the energy and the species equations while the PRESTO! scheme and the first-order upwind scheme are used for the pressure equation and the turbulence equations, respectively. Radiative heat transfer is accounted for using the discrete ordinates model and the weighted-sum-of-grey-gas model [22] using line-by-line and emissivity chart calculations. The radiative heat transfer equations neglect particle scattering and are solved for six pseudo gases and  $4 \times 8 \times 8$  directions using the finite volume method [62,63] and the first-order upwind scheme.

The gas reactions are described using the eddy-dissipation-concept model [64] and the reduced reaction mechanism for ethylene glycol using the rapid reduction method [65] from the most recent detailed mechanism for ethylene glycol [66]. Preceding works [24] already showed that this combined implementation provides reasonable near-flame and accurate far-flame predictions.

The fuel inlet is described differently compared to most of the preceding works [22,23,46–48,67–69]. Instead of the twin-fluid nozzle configuration, this work has adopted the free-jet nozzle approach with a simple circular orifice [24,49]. The corresponding nozzle diameter was derived using (i) the droplet velocities observed in the respective atomization and gasification experiments and (ii) the momentum flow rates of gas and liquid determined for the gasification experiment at nozzle inlet (see Appendix A.2 in supplementary material).

Infiltration air and purge nitrogen are not introduced through the nozzle as in previous works. Instead, source terms are incorporated into the continuity equation, the oxygen balance equation and the energy equation of some boundary layer cells while maintaining previous assumptions for the boundary conditions of the adiabatic top wall and of the heated side wall. Furthermore, temperatures of 1195 °C measured 50 mm below the surface of the side wall are applied within the common simplified thermal resistance approach. The wall thermal conductivity and the wall emissivity are defined with 2.22 W/(m K) and 0.8, respectively. Accordingly, the thermal boundary conditions at the wall were slightly changed as compared to the preceding works [24].

The liquid phase is injected using spherical droplets. The corresponding initial properties (see Appendix A.2 in supplementary material) were derived from the results of the PDA and patternator measurements (see Sections Section 2.3, 2.4 and 3.1). After injection, the droplets are tracked in the Lagrangian specification of reference. The trajectories are determined using the simplified transport equations for the droplet position, the droplet velocity, the droplet temperature and the droplet mass which (i) neglect particle interactions, (ii) account for gravity and thermal radiation, (iii) assume uniform droplet temperatures and (iv) describe vaporization based on the classical convective-diffusive vaporization model. Furthermore, turbulent dispersion is described using the discrete random walk model, the Morsi-Alexander equation [70] is applied for the drag coefficient, and the Ranz-Marshall equations [71,72] are used for the Nusselt and Sherwood numbers. The essential physical droplet properties are described using the PPDS and Wagner correlations for ethylene glycol [73].

### 3. Results

This section presents the results of the gasification and atomization experiments and the 2-Ph-FJM and CFD simulations. The cases A and B described in Section 2.1 are considered. Both cases have identical gas and liquid mass flow rates but differ in the gas exit area of the burner nozzles, resulting in a low and a high gas exit momentum.

The 2-Ph-FJM and the CFD model were validated using the results from the gasification experiments. Furthermore, the experimentally observed interdependence of different sub-processes was analyzed by the 2-Ph-FJM. The influence of fuel evaporation on the flame structure was investigated with the CFD model.

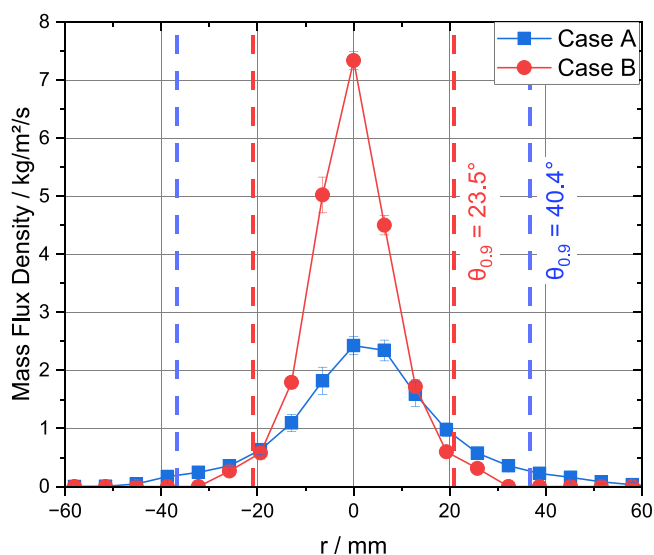


Fig. 2. Radial distribution of mass flux density for case A and B from the ambient patternator experiments at a nozzle distance of 100 mm.

#### 3.1. Spray characterization

Results on radial distribution of mass flux density in the ambient spray experiment at ATMO are shown for the two cases in Fig. 2. Mass balance errors were determined to be 8.5% and 11.5% for cases A and B respectively. Both nozzles show a bell-shaped distribution with case A exhibiting a wider spray angle. The difference in mass flux distribution is attributed to different liquid jet primary breakup patterns as shown by the high speed camera images in Fig. 3. Case A shows a flapping primary instability due to the low gas exit velocity of 69 m/s while for case B the high gas exit velocity of 156 m/s results in a super pulsating breakup of the primary liquid jet. These results are consistent with prior findings and theoretical work [74]. Based on this data, the factors for momentum exchange  $c_i$  as input parameters for the 2-phase free jet model were determined to be 0.0856 and 0.0776 for cases A and B respectively, according to [55]. The dashed lines in Fig. 3 represent the angle  $\theta_{0.9}$  accounting for 90% of the spray mass flow collected in the patternator experiment. The spray images from the gasification experiment indicate that the same spray patterns are present under reactive conditions. Therefore, it can be concluded that the patternator experiments provide reasonable input data for modeling the gasification experiments.

Radial distributions of the Sauter mean droplet diameter measured at ATMO under ambient conditions by PDA at  $z = 100$  mm are shown in Fig. 4. Both nozzles show profiles with increasing droplet size in the outer jet regions which is a typical feature of the applied atomizer design [75]. Case B generally has lower droplet sizes due to higher gas momentum flux at the nozzle exit compared to case A. Input conditions for modeling of the gasification experiments were defined based on this data.

To conclude, the increased gas exit momentum for case B leads to a narrower spray, smaller droplets and an overall higher entrainment rate due to the reduced nozzle equivalent diameter  $d_{eq}$  in comparison to case A.

#### 3.2. Experimental flame structure analysis

Fig. 5 shows OH-LIF and fuel tracer-LIF measurements at REGA. The spray distribution depicted in the fuel tracer-LIF images shows a broad spray distribution for case A with liquid fuel detected both inside and outside the oxidation zone (OZ, see Section 1.3), whereas for case B liquid fuel is only detected in a narrow region close to the jet axis.

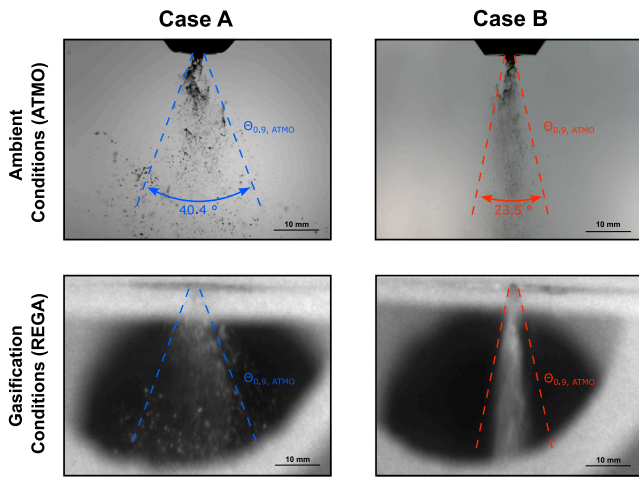


Fig. 3. Spray images under ambient and gasification conditions.

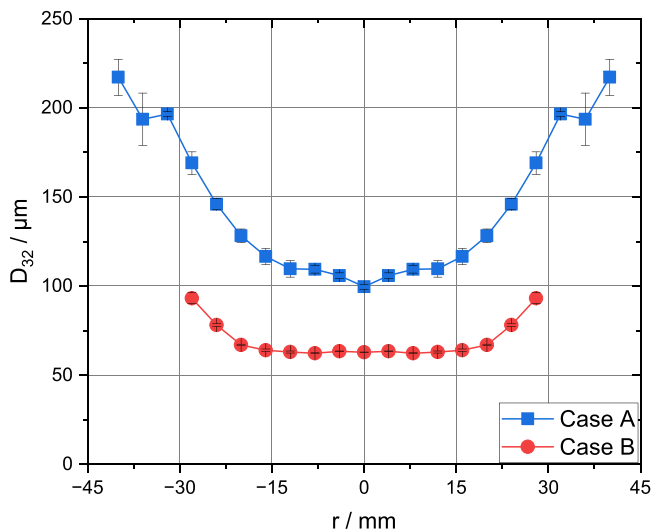


Fig. 4. Radial distributions of Sauter mean diameter under ambient conditions at a nozzle distance of 100 mm.

As indicated by the OH-LIF images, both flames show a distinct core zone (CZ) and have the same OZ structure in the region upstream the axial OH maximum. In the region downstream the OH maximum however, case A shows a compact long OZ whereas in case B a shorter, hollow cone shaped OZ is detected. This suggests an influence of the liquid fuel distribution on the spatial distribution of the OZ, which is further discussed together with the 2-Ph-FJM results in Section 3.3.

Since both nozzles have different gas exit cross-sections and thus different entrainment rates according to free jet theory, for discussion of flame length the equivalent nozzle diameter defined in Section 2.5 has to be considered. Fig. 6 shows radial profiles of OH-LIF intensity for four different normalized nozzle distances. The profiles close to the nozzle exit at  $z/d_{eq} = 5$  show the same M-shaped profile for both nozzles indicating oxidation reactions mainly at the jet boundaries, i.e. hot recirculated syngas reacting with oxygen rich gasification medium, while little oxidation is taking place at the jet axis at this point. At  $z/d_{eq} = 20$ , a bell-shaped OH profile is found for case A whereas case B still exhibits the M-profile with the highest OH-LIF intensities detected about 7 mm from the jet axis. For  $z/d_{eq} = 35$ , the shape of the OH-profiles remains unchanged but the profiles are broader and have lower intensities especially for case B. At a nozzle distance of  $z/d_{eq} = 47$ , there is still OH present for case A while almost no signal is detected for case B, which indicates a shorter oxidation zone under these conditions.

Gas temperature measurements shown in Fig. 7 support this statement. Comparison of radial temperature profiles at  $z/d_{eq} = 47$  generally show lower temperatures for case B, especially near the jet axis. This can be explained by the higher fuel concentration on the jet axis for case B which is further specified in chapter 3.3. Another notable difference between both temperature profiles is their general shape. For case A, a bell-shaped temperature distribution is clearly observed. For case B, the profile is flatter and no clear temperature maximum at the jet axis is found. An M-shaped profile with a temperature minimum near the jet axis is detected at  $z/d_{eq} = 35$ . This is consistent with the OH-LIF profiles acquired at the corresponding positions. The observed asymmetry of the profiles can be explained by infiltration air due to the invasive temperature measurement as well as by a slight flame asymmetry stemming from the burner nozzle as indicated by the OH-LIF profiles. However, these asymmetries do not compromise the general conclusions drawn from the measurements. With respect to differences in flame length and flame shape between the two cases, both OH-LIF and temperature measurement describe the same flame structure.

### 3.3. Two-phase free jet model

#### 3.3.1. Influence of spray angle

The experimentally observed influence of fuel spray distribution on length and shape of the OZ discussed in the previous chapter was further investigated using the 2-Ph-FJM. A parameter variation originating from case B was conducted modifying the radial liquid mass flow distribution. The parameters of the logistic function for mass flux density were changed to obtain different angles  $\theta_{0,9}$  ranging from  $15^\circ$  to  $40^\circ$  while keeping the integral liquid mass flow constant. Other input parameters of case B, particularly droplet size distribution, nozzle geometry and coefficients for turbulent exchange of momentum and mass were kept unchanged to ensure constant gas flow and mixing conditions.

Fig. 8 shows the resulting calculated temperature distributions. As can be seen, with decreasing  $\theta_{0,9}$  the temperature maximum on the jet axis moves closer towards the nozzle exit. In the region downstream the axial temperature maximum, the gas temperature gradient is steeper for the narrow sprays as compared to the wide sprays. For the two narrowest angles considered, a change in flame shape from compact to hollow cone is observed downstream the axial temperature maximum. In this case, the temperature profile shifts from a bell-shaped profile with maximal temperature on the jet axis to an M-profile. The axial temperatures are significantly reduced and the highest temperatures are now found off the jet axis.

These two observations are consistent with the statements on flame length and flame shape derived from the gasification experiments on the basis of OH- and temperature distribution in Section 3.2. Fig. 9 provides an explanation for this behavior by showing oxygen mole fraction and absolute gas phase stoichiometry calculated by the 2-Ph-FJM on the jet axis. In general, a core region with a constant oxygen mole fraction can be observed at the jet axis up to an axial nozzle distance of approximately 50 mm for both cases. When syngas from the gasification zone reaches the jet axis through turbulent mixing at this distance, oxygen mole fraction decreases due to reaction of the jet medium (oxidizer) with entrained syngas, indicating the start of the oxidation zone. The temperature increase causes evaporation of fuel droplets to start at approximately 55 mm, which results in additional oxygen consumption by the fuel vapor now available in the gas phase. From this point, a difference between the two cases is observed for the different fuel spray distributions. Narrowing the spray from  $\theta_{0,9} = 40^\circ$  to  $15^\circ$  leads to a higher concentration of liquid fuel on the jet axis. Downstream the starting point of droplet evaporation, this results in more gaseous fuel being available on the jet axis, which is reflected by lower values of  $\lambda_{abs}$  for the  $15^\circ$  case. The increased availability of fuel vapor results in a faster consumption of oxygen

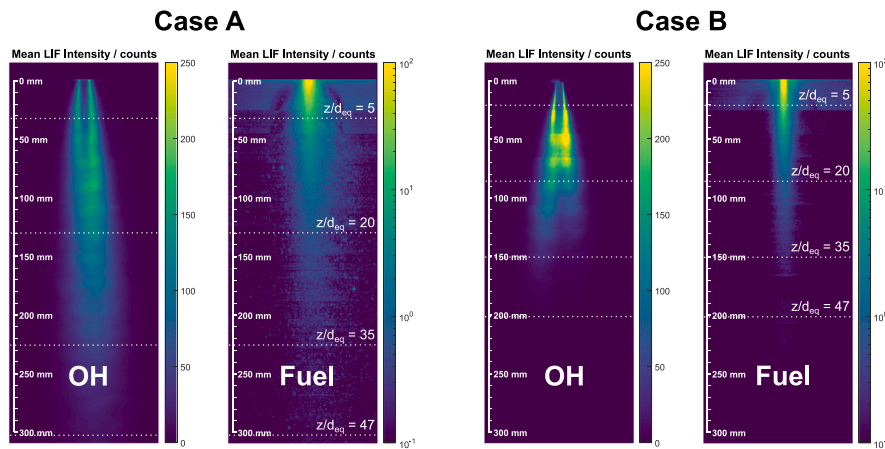


Fig. 5. Flame structure and fuel distribution results for cases A and B. Left images show averaged OH-LIF signal, right images show averaged fuel tracer LIF signal.

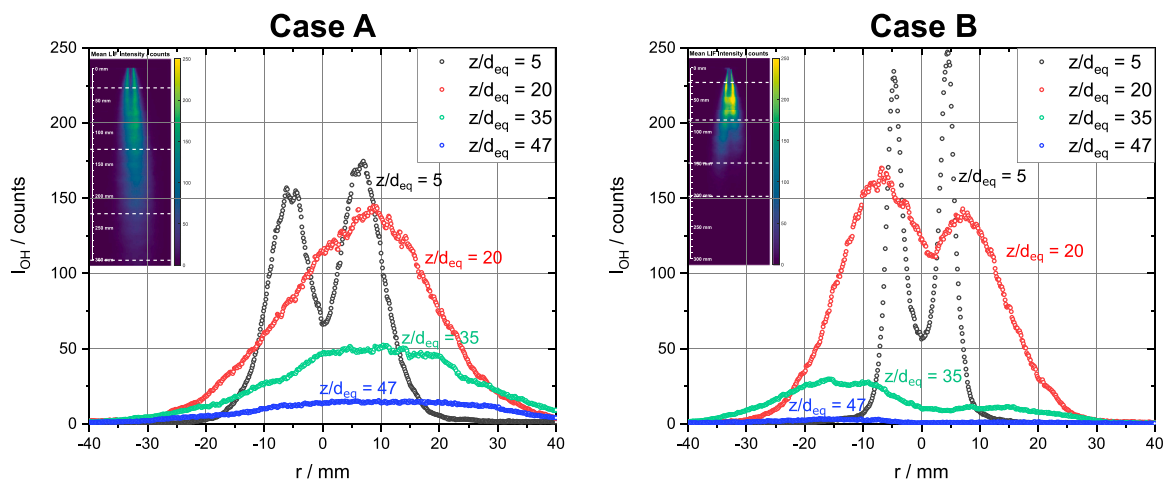


Fig. 6. OH-LIF radial profiles for cases A and B at 4 different nondimensional nozzle distances.

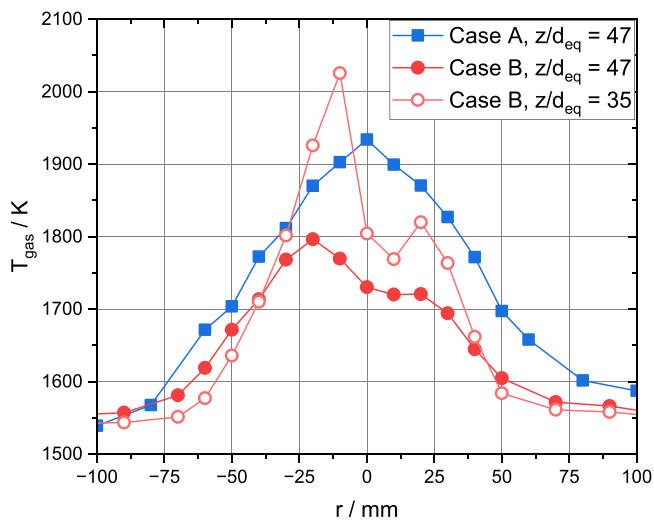


Fig. 7. Temperature profiles for case A and B for different nondimensional nozzle distances.

compared to the wider spray case, leading to heat release by oxidation being completed at a shorter nozzle distance. Additionally, further fuel evaporation after complete oxygen consumption leads to further cooling of the gas phase in the gasification zone. This is caused by evaporation cooling and endothermic gasification reactions under now oxygen free atmosphere, causing the faster temperature decline for smaller spray angles observed in Fig. 8.

For very narrow sprays, this effect concentrates on the jet axis and leads to the observed difference in flame shape, as Fig. 10 shows. Here, radial profiles of temperature and local stoichiometry are displayed for three different  $\theta_{0.9}$  and the original case B at  $z/d_{eq} = 35$ . Narrowing the spray to very small angles leads to a minimum of local stoichiometry on the jet axis, causing a corresponding minimum of gas temperature, as can be seen for the 15° and 20° case. In the 25° case, a bell-shaped stoichiometry and temperature profile is obtained. In the outer region, temperatures below the ambient temperature can be detected. This is attributed to the fact that for broader sprays, a significant portion of the droplets move on trajectories outside the gas jet, in the gasification zone. These droplets cool the ambient gas due to evaporation and endothermic gasification reactions.

### 3.3.2. Validation of 2-phase free jet simulations

For comparison, temperature fields simulated by 2-Ph-FJM for the cases A and B are displayed in Fig. 11. In contrast to the isolated variation of spray distribution in the previous chapter, these simulations also

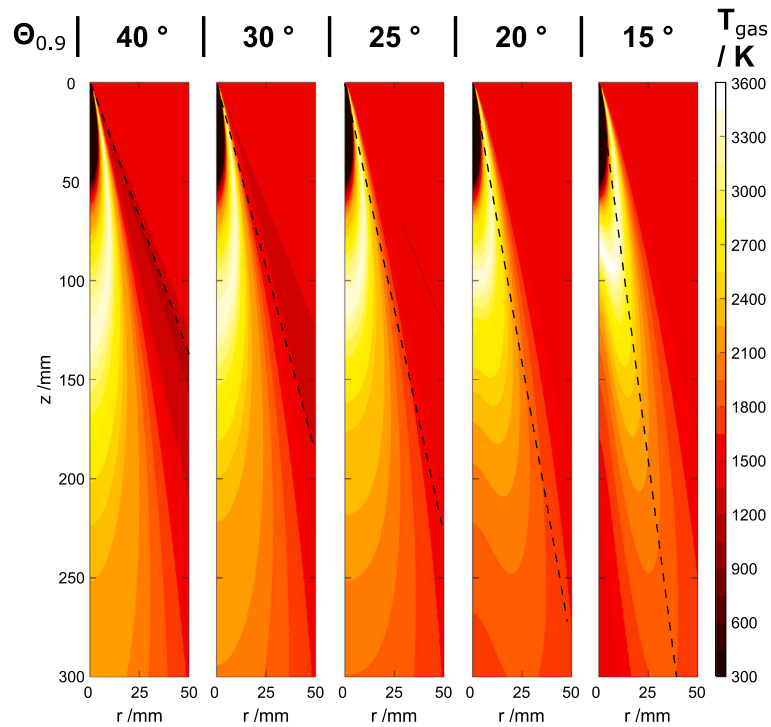


Fig. 8. Calculated temperature fields for case B input parameters with different radial spray distributions (Free Jet Model).

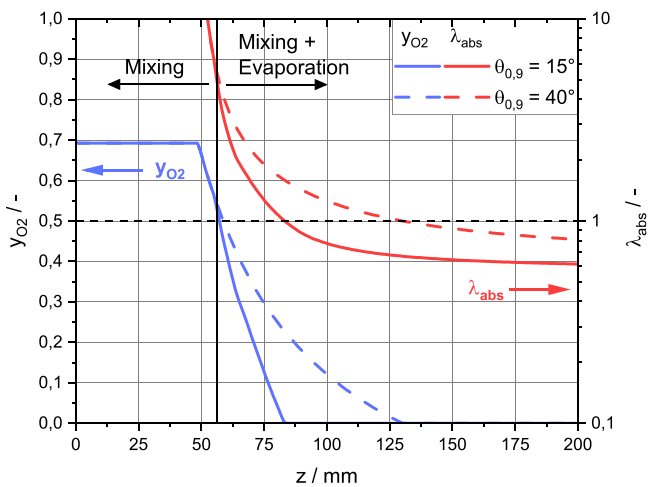


Fig. 9. Oxygen mole fraction and local absolute stoichiometry on the jet axis calculated for two different radial spray distributions in the 2-Ph-FJM sensitivity study.

include the effects of the different nozzle diameters and droplet size distributions for the two cases. As can be seen in comparison with the measured gas temperature profiles in Fig. 7 and the OH images in Fig. 5, the compact flame shape for case A is predicted correctly. The bell-shaped temperature profile observed in the experiments is qualitatively reproduced by the model, which exhibits a temperature maximum on the jet axis in the downstream flame region. The modeled bell shape is also consistent with the OH-LIF results. The lower temperature outside the jet boundaries in the gasification zone however is not found experimentally. This discrepancy is due to the modeling of the atomization process, where the droplets outside the gas jet boundaries have low velocities and therefore long residence times. This leads to a temperature reduction in the gasification zone due to fuel evaporation and endothermic reactions. In the physical atomization process in contrast, the flapping primary jet breakup produces faster droplets with

high momentum in the outer spray regions leading to the fuel droplets to be more evenly distributed in the recirculation zone.

For case B, the modeled flame is shorter than for case A as indicated by the lower temperature at  $z/d_{eq} = 47$ , which is in agreement with the OH and temperature measurements. This is caused by the increased availability of fuel vapor in the gas jet because of a narrower fuel spray and smaller droplets, leading to faster evaporation compared to case A. Case B can be seen as a transition between the compact and the hollow cone flame shapes which occurs in the range of  $\theta_{0.9} = 20^\circ$  to  $25^\circ$ , as Figs. 10 and 8 show. Case B with  $\theta_{0.9} = 23.5^\circ$  is set in between and still exhibits a bell-shaped temperature profile, which is in contrast to the experimentally determined temperature profiles in Fig. 7. For a slightly smaller  $\theta_{0.9}$  however, the profile shows the temperature distribution expected from the experiment, leading to the correct flame shape (Fig. 10). Since the reaction model is constrained to main species, high temperature dissociation to radicals is not accounted for. Therefore, the model overpredicts gas temperature in hot regions and a temperature comparison between model and experiment can only be made on a qualitative level.

To conclude, the 2-Ph-FJM clearly shows the influence of fuel spray distribution on oxidation zone structure in an EFG inverse diffusion flame by enabling an independent variation of fuel spray distribution and gas phase mixing. The free jet model achieves its goals of capturing the relevant effects and providing an explanation for the observed behavior, allowing qualitative statements about the interaction between fuel spray and oxidizer under conditions typical for EFG to be made.

### 3.4. CFD simulations

RANS based CFD simulations for gasification are known to provide accurate far-flame predictions of gas temperature and gas concentrations in reasonable computing time [22]. This can be achieved for case B at a nozzle distance of 680 mm. Gas temperature and dry gas concentrations shown in Figs. 12 and 13 are in good agreement with previous experimental results [76].

However, it is also interesting to investigate the near-flame predictions of RANS based CFD simulations and to determine how far the



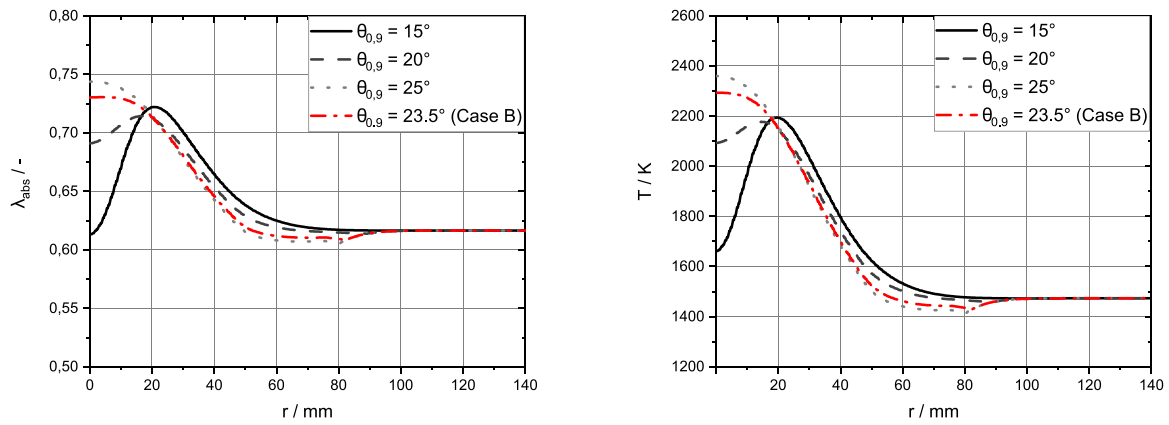


Fig. 10. Calculated radial distributions of local absolute stoichiometry (left) and gas temperature (right) for 3 different radial spray distributions at  $z/d_{eq} = 35$ . Model results for case B are shown for reference.

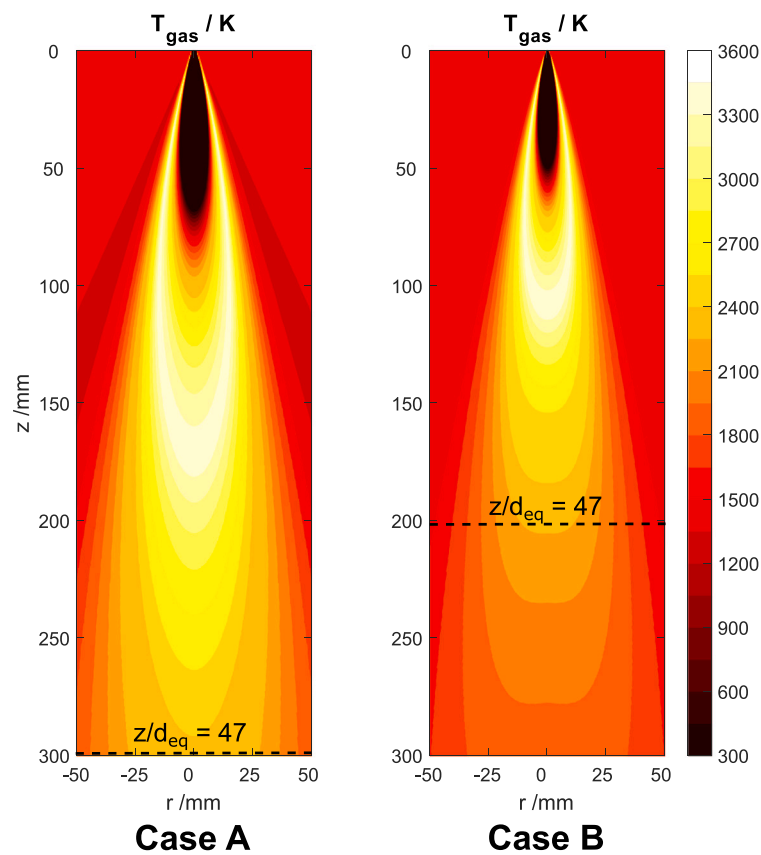


Fig. 11. Temperature fields for case A (left) and B (right) calculated by the 2-Ph-FJM.

experimental observations can be accounted for in spite of deficiencies in turbulence, turbulence dispersion and turbulence-chemistry interaction models. Concerning the radial gas temperature profiles at a nozzle distance of 300 mm, limited agreement is observed in Figs. 14 and 15.

This can be explained by the insufficient mathematical description of the fuel mass transfer into the gas phase. If the common film factor of 1/3 (for example, see [77–79]) in the vaporization model is changed to 1, the fuel mass transfer from droplet to gas phase is accelerated providing predictions that are in better agreement with the experimental observations. Accordingly, the actual atomization and turbulence processes lead to stronger turbulent mixing of the fuel and the gasification medium and to longer droplet residence times in the flame region and, thus, to faster fuel mass transfer into the gas phase than obtained by the RANS based CFD simulations. Therefore, the

predicted colder core zones shown in Fig. 16 are significantly longer than it is observed experimentally (see Section 3.2) or can be predicted using large eddy simulations (see [23,67]).

However, the flame shapes that are indicated by the OH-LIF measurements (see Section 3.2) are predicted quite well for both cases when applying 1/3 as film factor. Numerical results of gas temperature and OH mole fraction in Figs. 16 and 17, respectively, indicate bell-shaped OH and gas temperature radial profiles for case A and M-shaped profiles for case B, which also confirms the results of the 2-phase free-jet simulations (see Section 3.3). However, if the film factor of 1/3 is changed to 1 to enhance the fuel mass transfer, the flame shape significantly changes for case A as shown in Fig. 18. Together with the broad droplet size distribution (Appendix A.2 in supplementary material), this can be attributed to the injection properties of the fuel

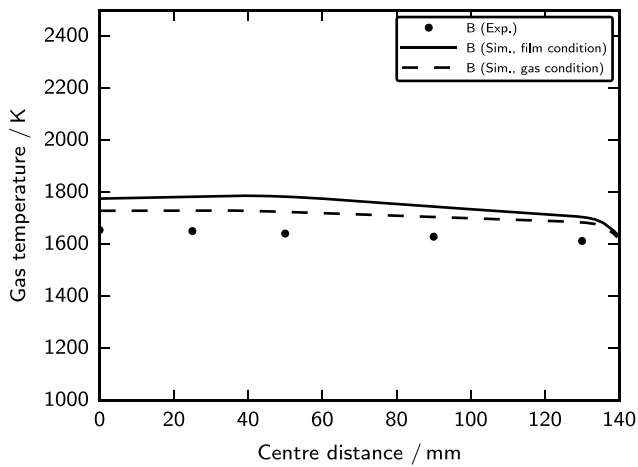


Fig. 12. Radial profiles of the gas temperature for case B at a nozzle distance of 680 mm. Exp.: experimental results [76]; Sim., film condition: numerical results obtained using the 1/3 rule for the film properties; Sim., gas condition: numerical results obtained using the gas condition for the film properties.

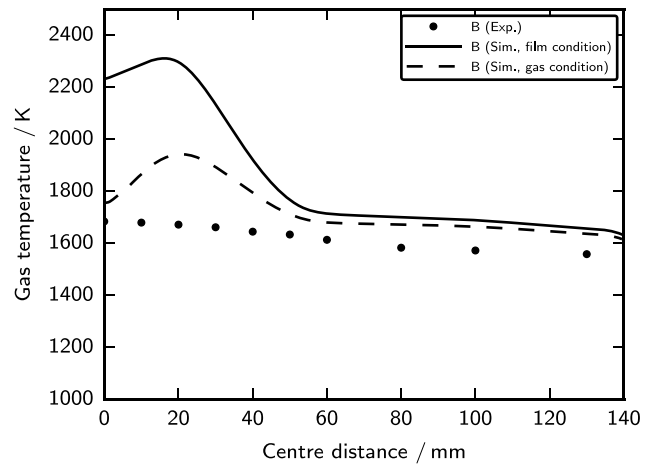


Fig. 15. Radial profiles of gas temperature for case B at a nozzle distance of 300 mm. Exp.: experimental results; Sim., film condition: numerical results obtained using the 1/3 rule for the film properties; Sim., gas condition: numerical results obtained using the gas condition for the film properties.

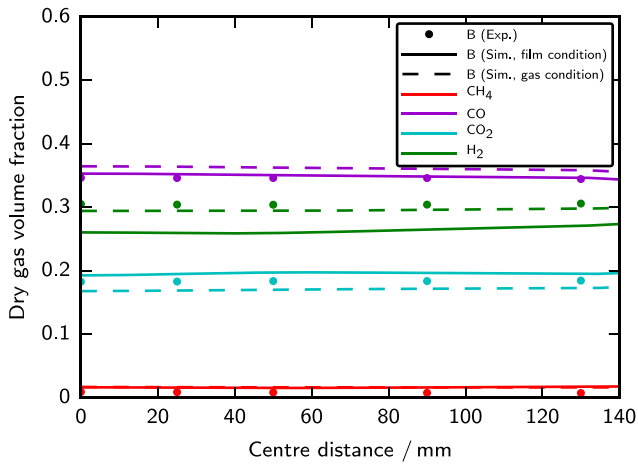


Fig. 13. Radial profiles of the dry gas volume fractions for case B at a nozzle distance of 680 mm. Exp.: experimental results [76]; Sim., film condition: numerical results obtained using the 1/3 rule for the film properties; Sim., gas condition: numerical results obtained using the gas condition for the film properties.

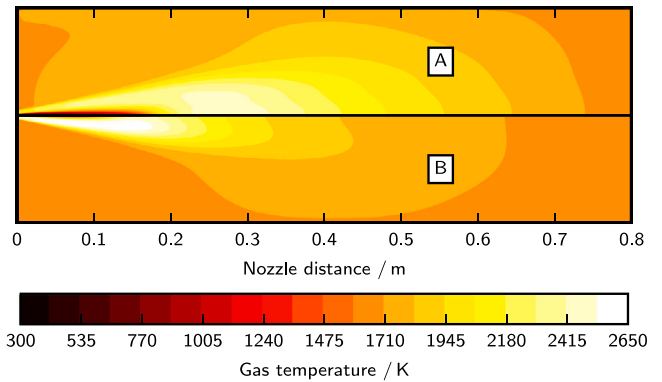


Fig. 16. Numerical gas temperature distribution using the 1/3 rule for the film properties. A: results for case A; B: results for case B.

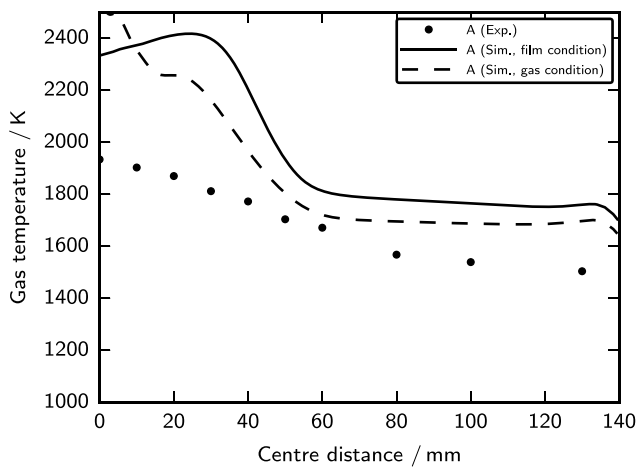


Fig. 14. Profiles of the gas temperature for case A at a nozzle distance of 300 mm. Exp.: experimental results; Sim., film condition: numerical results obtained using the 1/3 rule for the film properties; Sim., gas condition: numerical results obtained using the gas condition for the film properties.

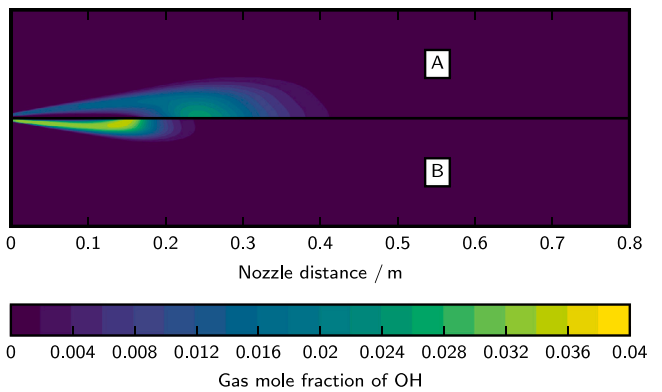


Fig. 17. Numerical gas mole fraction distribution of OH using the 1/3 rule for the film properties. A: results for case A; B: results for case B.

droplets in combination with insufficient turbulent mixing. Since the number of injection events was limited for computing time reasons, 13 injection positions were assumed corresponding to 13 directions with mean initial droplet velocities (Appendix A.2 in supplementary

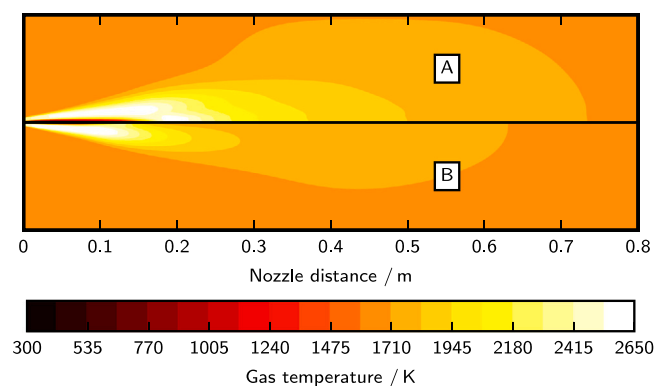


Fig. 18. Numerical gas temperature distribution using the gas condition for the film properties. A: results for case A; B: results for case B.

material). This lead to some discontinuities in the fuel spray distribution and to the discontinuous flame for case A when applying 1 as film factor. Further injections might slightly improve the near-flame predictions but increase the computing time. Therefore, elaborative approaches (for example, based on large eddy simulations combined with the volume-of-fluid method) may support future RANS based CFD simulations with injection properties and models that improve the description of turbulent mixing, fuel spray distribution and fuel conversion.

#### 4. Summary

The impact of the fuel spray distribution on the structure of an inverse diffusion flame in an entrained flow gasifier was investigated by experiments and modeling.

Two nozzles with different gas exit momentum were applied under identical operating conditions to obtain different radial spray distributions. A comprehensive dataset was generated by measuring fuel spray distribution under atmospheric and gasification conditions, followed by flame structure analysis using OH-LIF and temperature measurements in an atmospheric entrained flow gasifier. For analysis of the spatial distribution of the reaction zones in the flame, a core zone, an oxidation zone and a gasification zone were defined. The experimental results indicate that the axial and radial extension of the oxidation zone is determined by the fuel spray distribution. A narrower fuel spray distribution leads to a shorter oxidation zone and to a transition from a compact to a hollow cone structure in the downstream flame region.

The experiments were accompanied by simulations using a 2-phase free-jet model and a RANS based CFD model, which were adopted from preceding works and modified to account for the fuel spray distributions observed in the spray characterization experiments. The near-flame predictions using both models qualitatively reflect the experimentally observed flame shapes, the far-flame predictions using the RANS based CFD model are in good quantitative agreement with the experimental observations.

A numerical analysis using the two-phase free-jet model shows that the fuel spray distribution affects the local stoichiometry which is decisive for the flame structure. The model is able to qualitatively describe the observed flame structure and provide a deeper understanding of the interacting sub-processes. Further analysis with the CFD model support the conclusions drawn from the 2-phase free-jet simulations and show the importance of the fuel mass transfer into the gas phase.

Future experimental work should clarify the implications of the observed fuel spray distribution effects on the gasification of technical liquid and suspension fuels. Since more advanced models cannot be applied in the foreseeable future to describe technical fuels characterized by complex compositions, future modeling work needs to focus on the adaption of the 2-phase free-jet model and the RANS based CFD model to technical fuels to derive a deeper process understanding.

#### CRediT authorship contribution statement

**Manuel Haas:** Conceptualization, Methodology, Software, Validation, Investigation, Writing – original draft. **Maximilian Dammann:** Methodology, Software, Investigation, Writing – original draft. **Sabine Fleck:** Conceptualization, Writing – review and editing, Methodology, Investigation, Supervision. **Thomas Kolb:** Conceptualization, Writing – review and editing, Supervision, Project administration.

#### Declaration of competing interest

The authors declare that they have no known competing financial interests or personal relationships that could have appeared to influence the work reported in this paper.

#### Data availability

Data will be made available on request.

#### Acknowledgments

The authors gratefully acknowledge the financial support by the Helmholtz Association of German Research Centers (HGF) in the context of the research program Materials and Technologies for the Energy Transition (MTET). The present work contributes to the Helmholtz Virtual Institute for Gasification Technology–HVIGasTech (VH-VI-429) (<http://www.hvigastech.org/>). The authors thank Christian Hotz (formerly Karlsruhe Institute of Technology, Institute for Technical Chemistry, Gasification Technology), Marco Mancini and Roman Weber (Clausthal University of Technology, Institute for Energy Process Engineering and Fuel Technology) and Michael Alberti (formerly Clausthal University of Technology, Institute for Energy Process Engineering and Fuel Technology) for their preceding works and the constant collaboration.

#### Appendix A. Supplementary data

Supplementary material related to this article can be found online at <https://doi.org/10.1016/j.fuel.2022.126572>.

#### References

- [1] Kolb T, Aigner M, Kneer R, Müller M, Weber R, Djordjevic N. Tackling the challenges in modelling entrained-flow gasification of low-grade feedstock. *J Energy Inst* 2016;89(4):485–503. <http://dx.doi.org/10.1016/j.joei.2015.07.007>.
- [2] Fleck S, Santo U, Hotz C, Jakobs T, Eckel G, Mancini M, et al. Entrained flow gasification. Part 1: gasification of glycol in an atmospheric-pressure experimental rig. *Fuel* 2018;217:306–19. <http://dx.doi.org/10.1016/j.fuel.2017.12.077>.
- [3] Azuhata S, Hedman PO, Smoot LD, Sowa WA. Effects of flame type and pressure on entrained coal gasification. *Fuel* 1986;65(11):1511–5. [http://dx.doi.org/10.1016/0016-2361\(86\)90326-1](http://dx.doi.org/10.1016/0016-2361(86)90326-1).
- [4] Sowa WA, Hedman PO, Smoot LD, Richards DO. The sensitivity of entrained-flow coal gasification diffusion burners to changes in geometry. *Fuel* 1992;71(5):593–604. [http://dx.doi.org/10.1016/0016-2361\(92\)90159-L](http://dx.doi.org/10.1016/0016-2361(92)90159-L).
- [5] Kidoguchi K, Hara S, Ashizawa M, Inumaru J. Study on extra heavy oil gasification reaction process. *JSME Int J Ser B Fluids Therm Eng* 2002;45(3):523–9. <http://dx.doi.org/10.1299/jsmeb.45.523>.
- [6] Parameswaran T, Duchesne MA, Champagne S, Hughes RW. Petroleum coke gasification temperatures and flame spectra in the visible region at high pressure. *Energy Fuels* 2016;30(11):9867–75. <http://dx.doi.org/10.1021/acs.energyfuels.6b01751>.
- [7] Song X, Guo Q, Hu C, Gong Y, Yu G. Optical experimental study on the characteristics of impinging coal-water slurry flame in an opposed multi-burner gasifier. *Fuel* 2017;188:132–9. <http://dx.doi.org/10.1016/j.fuel.2016.10.028>.
- [8] Qin K, Jensen PA, Lin W, Jensen AD. Biomass gasification behavior in an entrained flow reactor: gas product distribution and soot formation. *Energy Fuels* 2012;26(9):5992–6002. <http://dx.doi.org/10.1021/ef300960x>.
- [9] Wu X, Guo Q, Gong Y, Liu J, Luo X, Wu T, et al. Influence of burner geometry on atomization of coal water slurry in an entrained-flow gasifier. *Chem Eng Sci* 2022;247:117088. <http://dx.doi.org/10.1016/j.ces.2021.117088>.



- [58] ANSYS. ANSYS fluent release R2020.2. 2020, URL <https://www.ansys.com/products/fluids/ansys-fluent>.
- [59] Menter FR. Two-equation eddy-viscosity turbulence models for engineering applications. *AIAA J* 1994;32(8):1598–605. <http://dx.doi.org/10.2514/3.12149>.
- [60] Menter FR, Kuntz M, Langtry R. Ten years of industrial experience with the SST turbulence model. *Turbul Heat Mass Transf* 2003;4(1):625–32.
- [61] Patankar SV, Spalding DB. A calculation procedure for heat, mass and momentum transfer in three-dimensional parabolic flows. *Int J Heat Mass Transfer* 1972;15(10):1787–806. [http://dx.doi.org/10.1016/0017-9310\(72\)90054-3](http://dx.doi.org/10.1016/0017-9310(72)90054-3).
- [62] Chui EH, Raithby GD. Computation of radiant heat transfer on a nonorthogonal mesh using the finite-volume method. *Numer Heat Mass Transfer B* 1993;23(3):269–88. <http://dx.doi.org/10.1080/10407799308914901>.
- [63] Murthy JY, Mathur SR. Finite volume method for radiative heat transfer using unstructured meshes. *J Thermophys Heat Transfer* 1998;12(3):313–21. <http://dx.doi.org/10.2514/2.6363>.
- [64] Magnussen B. On the structure of turbulence and a generalized eddy dissipation concept for chemical reaction in turbulent flow. In: *Proceedings of the 19th aerospace sciences meeting*. (81–31510); St. Louis, MO, USA: American Institute of Aeronautics and Astronautics; 1981, p. 1–6. <http://dx.doi.org/10.2514/6.1981-42>.
- [65] Methling T, Kathrotia T, Riedel U. Rapid reduction of a chemical kinetic model for the combustion of the pyrolysis oil surrogate ethylene glycol. In: *Proceedings of the 16th international conference on numerical combustion*. Orlando, FL, USA; 2017.
- [66] Kathrotia T, Naumann C, Oßwald P, Köhler M, Riedel U. Kinetics of ethylene glycol: the first validated reaction scheme and first measurements of ignition delay times and speciation data. *Combust Flame* 2017;179:172–84. <http://dx.doi.org/10.1016/j.combustflame.2017.01.018>.
- [67] Eckel G. Large eddy simulation of turbulent reacting multi-phase flows (Ph.D. thesis), Stuttgart, Germany: Universität Stuttgart, Fakultät für Luft- und Raumfahrttechnik und Geodäsie, Universität Stuttgart; 2018, <http://dx.doi.org/10.18419/opus-9941>.
- [68] Fradet Q, Braun-Unkhoff M, Riedel U. A sectional approach for the entrained-flow gasification of slurry fuels. *Energy Fuels* 2018;32(12):12532–44. <http://dx.doi.org/10.1021/acs.energyfuels.8b02785>.
- [69] Fradet Q. Novel modeling approaches for the entrained-flow gasification of bio-slurries (Ph.D. thesis), Stuttgart, Germany: Fakultät für Luft- und Raumfahrttechnik und Geodäsie, Universität Stuttgart; 2020, <http://dx.doi.org/10.18419/opus-10989>.
- [70] Morsi SA, Alexander AJ. An investigation of particle trajectories in two-phase flow systems. *J Fluid Mech* 1972;55(2):193–208. <http://dx.doi.org/10.1017/s0022112072001806>.
- [71] Ranz WE, Marshall WR. Evaporation from drops. Part I. *Chem Eng Progr* 1952;48(3):141–6.
- [72] Ranz WE, Marshall WR. Evaporation from drops. Part II. *Chem Eng Progr* 1952;48(3):173–80.
- [73] VDI-Gesellschaft Verfahrenstechnik und Chemieingenieurwesen (VDI-GVC). VDI-wärmeatlas, In: Stephan P, Kabelac S, Kind M, Martin H, Mewes D, Schaber K, editors. 11th ed.. Berlin, Germany: Springer; 2013, <http://dx.doi.org/10.1007/978-3-642-19981-3>.
- [74] Lasheras JC, Hopfinger E. Liquid jet instability and atomization in a coaxial gas stream. *Annu Rev Fluid Mech* 2000;32(1):275–308. <http://dx.doi.org/10.1146/annurev.fluid.32.1.275>.
- [75] Wächter S, Jakobs T, Kolb T. Towards system pressure scaling of gas assisted coaxial burner nozzles—an empirical model. *Appl Energy Combust Sci* 2021;5:100019. <http://dx.doi.org/10.1016/j.jaecs.2020.100019>.
- [76] Fleck S, Haas M, Santo U, Kolb T. Entrained flow gasification glycol-beech wood-char slurry in an atmospheric-pressure experimental rig. *Fuel* 2023. [in preparation].
- [77] Yuen MC, Chen LW. On drag of evaporating liquid droplets. *Combust Sci Technol* 1976;14(4–6):147–54. <http://dx.doi.org/10.1080/00102207608547524>.
- [78] Abramzon B, Sirignano WA. Droplet vaporization model for spray combustion calculations. *Int J Heat Mass Transfer* 1989;32(9):1605–18. [http://dx.doi.org/10.1016/0017-9310\(89\)90043-4](http://dx.doi.org/10.1016/0017-9310(89)90043-4).
- [79] Stöhr M, Ruoff S, Rauch B, Meier W, Le Clercq P. Droplet vaporization for conventional and alternative jet fuels at realistic temperature conditions: Systematic measurements and numerical modeling. *Proc Combust Inst* 2021;38(2):3269–76. <http://dx.doi.org/10.1016/j.proci.2020.05.015>.